Potential Vorticity Diagnosis of a Tropopause Polar Cyclone

STEVEN M. CAVALLO AND GREGORY J. HAKIM

University of Washington, Seattle, Washington

ABSTRACT

Long-lived coherent vortices located near the tropopause are often found over polar regions. Although these vortices are a commonly observed feature of the Arctic, and can have lifetimes longer than one month, little is known about the mechanisms that control their evolution. This paper examines mechanisms of intensity change for a cyclonic tropopause polar vortex (TPV) using an Ertel potential vorticity (EPV) diagnostic framework. Results from a climatology of intensifying cyclonic TPVs suggest that the essential dynamics are local to the vortex, rather than a consequence of larger-scale processes. This fact motivates a case study using a numerical model to investigate the role of diabatic mechanisms in the growth and decay of a particular cyclonic vortex. A component-wise breakdown of EPV reveals that cloud-top radiational cooling is the primary diabatic mechanism that intensifies the TPV during the growth phase. Increasing amounts of moisture become entrained into the vortex core at later times near Hudson Bay, allowing the destruction of potential vorticity near the tropopause due to latent heat release to become comparable to the radiational tendency to create potential vorticity.

1. Introduction

Tropopause vortices are extratropical, cold-core cyclones or warm-core anticyclones, defined by closed material contours. On the dynamic tropopause, taken to be a potential vorticity (PV) surface, cyclones are characterized by relatively high pressure (lowered tropopause) and low potential temperature while anticyclones are characterized by relatively low pressure (raised tropopause) and high potential temperature. The Arctic is particularly favorable for these features, with relatively weak vertical and horizontal wind shear providing an environment conducive for vortex longevity. Horizontal length scales of these tropopause polar vortices (TPVs) are most often less than 1000 km in radius, and their life span can extend beyond one month (Hakim and Canavan 2005). Despite their ubiquity and longevity, little is known about the mechanisms that control their evolution. This study focuses on mechanisms affecting cyclonic vortex intensity, and specifically examines the life cycle of an observed event using a numerical model and a PV diagnostic framework.

In the context of PV, vortex amplitude on the dynamic tropopause can be defined by the range of closed contours of potential temperature.[1] Therefore, changes in vortex strength require nonconservative diabatic or frictional processes (e.g., Pedlosky 1998, his section 2.5). This PV perspective has been applied extensively to studies of warm-core cyclones, where significant latent heating has been shown to affect vortex intensity (e.g., Shapiro and Willoughby 1982; Schubert and Hack 1983; Nolan and Grasso 2003). In these cases, latent heating produces low-level PV, which intensifies the vortex in regions near where the vortices are strongest.

Several studies have addressed the effect of diabatic processes on the PV distribution near extratropical cyclones. For example, Davis and Emanuel (1991) used a piecewise PV inversion methodology in a case study quantifying the development of a low-level PV anomaly produced by latent heating. They found that this low-level PV anomaly subsequently contributed to the reduction of downstream tropopause-level PV, and suggested that in addition to advection, destruction due to

Corresponding author address: Steven Cavallo, Department of Atmospheric Sciences, University of Washington, Box 351640, Seattle, WA 98195-1640.
E-mail: scavallo@atmos.washington.edu

---

[1] Assuming adiabatic and inviscid flow, PV and potential temperature are both conserved following the fluid motion. Thus, the existence of closed PV contours on potential temperature surfaces implies the existence of closed contours of potential temperature on PV surfaces.

latent heating could also have been an important mechanism in amplifying downstream PV. Using a similar technique in a numerical modeling study, Stoelinga (1996) showed that latent heating destroyed upper-level PV downstream and above the latent heating source in the direction of the absolute vorticity vector, consistent with theoretical expectations.

Few studies have examined the effect of nonconservative PV processes on the dynamics of isolated cold-core extratropical vortices. Cold-core cyclonic vortices strengthen upward in the troposphere, and since low-level latent heating typically destroys upper-level PV, latent heating leads to a weaker vortex (e.g., Hoskins et al. 1985, their section 7). For example, Wirth (1995) performed an idealized study of an axisymmetric tropopause cyclone and found that a latent heat source located in the cyclone core acted to weaken the vortex considerably. Adding an idealized thin layer of modest cooling to simulate the effect of cloud-top radiational cooling had little effect on the cyclone evolution. However, increasing the magnitude of the cloud-top radiational cooling strengthened the vortex, suggesting that radiation may play a role in cyclonic vortex intensity change, depending on the exact magnitude and location of the cloud-top radiational cooling relative to the tropopause (Wirth 1995). Idealized radiational cooling in isolation was shown in a subsequent idealized study of an axisymmetric anticyclonic vortex to create upper-level PV and lower the tropopause (Zierl and Wirth 1997). The combined interactive effects of latent heating and cloud-top radiational cooling on vortex intensity do not appear to have been previously considered.

Hakim and Canavan (2005) performed an objective census of tropopause vortices and found an average of 15 unique cyclonic vortices per month, with a frequency maximum over the Canadian Arctic. Here we extend these results by examining the vortex census results of Hakim and Canavan (2005) to identify regions of TPV genesis, growth, and decay. A numerical simulation of a particular case is then analyzed from a PV framework with the goal of investigating how diabatic and radiational processes affect vortex strength.

This paper is organized as follows. Section 2 provides a brief climatology of cyclonic TPV genesis and intensity change, the results of which suggest that the essential dynamics are local to the vortex rather than dependent on large-scale patterns. This finding motivates the use of PV diagnostics on a numerical simulation of a particular case. The theory and methodology for the PV diagnostics are described in section 3, and an overview of the case study is provided in section 4. A description of the numerical model and model simulation results from the case study, including a PV budget,

are provided in section 5. A concluding summary is given in section 6.

2. Tropopause polar vortex climatology of intensification

Vortices are identified here by the presence of closed contours of potential temperature on the dynamic tropopause (e.g., Hakim 2000), defined by a PV surface. Adiabatic conditions imply that fluid parcels located within closed contours act as tracers of the vortex. A change in the range of closed potential temperature contours on the PV surface representing the tropopause provides one objective measure of vortex amplitude change, and we employ this method in our analysis. Using the vortex dataset of Hakim and Canavan (2005), we extend the results of their climatology in this section to examine a TPV climatology of intensification, with the goal of determining where vortex intensification occurs and whether there exists a relationship between intensification and large-scale flow patterns.

Regions of cyclonic TPV intensity change are determined from 2.5° National Centers for Environmental Prediction–National Center for Atmospheric Research (NCEP–NCAR) reanalysis data every 6 h during 1948–99 (Kalnay and collaborators 1996). Tropopause vortices are identified and tracked using an objective algorithm developed and described in Hakim and Canavan (2005), which tracks TPVs on the 1.5 PVU (1 PVU $\equiv$ 1×10^{-6} K kg^{-1} s^{-1} m^2) PV surface. Cyclonic vortex amplitude, defined as the difference between the local minimum in potential temperature (which we call the core value) and the last closed contour, is used to determine the strength of the vortices relative to their surroundings. TPVs are defined as in Hakim and Canavan (2005) to include only those vortices that spend at least 60% of their lifetime north of 65°N and last at least 2 days. To filter out spurious intensity changes, we discard any event for which there is a tropopause potential temperature amplitude change of at least 10 K followed by an amplitude change of at least 75% of the opposite sign within the following 12 h; this eliminates about 2% of the vortices. Although an arbitrary threshold, high-frequency amplitude changes such as these are considered to be numerical artifacts, beyond the range of observed EPV tendency attributable to diabatic tendencies (e.g., Davis and Emanuel 1991; Davis 1992; Stoelinga 1996). Vortex genesis is defined to occur by the identification of a local minimum in tropopause potential temperature that is colder than all other locations within a 650-km radius, which is roughly the vortex length scale; results are not sensitive to this radius. Vortex lysis is defined to occur when a local minimum in tropopause

potential temperature can no longer be identified with an existing vortex track. Growth (decay) refers to the greatest increase (decrease) in amplitude during a 24-h period over the vortex lifetime.

Results show that TPV genesis occurs most frequently in the Canadian archipelago and northern Baffin Bay, with less dense areas located along the northern Siberian coast (Fig. 1a). In general, cyclolysis densities are greatest just downstream of the maximum tropopause cyclogenesis regions, with the greatest density near the northwestern coast of Greenland and along the coast of northern Siberia near Severnaya Zemlya (Fig. 1b). Cyclone growth occurs most often near northern Baffin Island, with a secondary maximum over central Greenland, and smaller maxima along the northern coast of Siberia (Fig. 1c). Cyclone decay occurs most frequently over northern Baffin Island, with a secondary maximum over eastern Greenland (Fig. 1d). The close proximity of the main TPV cyclogenesis and cyclolysis regions suggests that vortices form and spend most their lifetime in the same region.

To pursue the possibility of large-scale circulation anomalies associated with tropopause cyclone intensification, a compositing analysis of NCEP–NCAR reanalysis 500-hPa geopotential heights is performed for the 264 cases occurring within a 5° latitude and 15° longitude box centered at (70°N, 74°W), the location where maximum tropopause cyclone growth occurs. Statistical significance is assessed by a two-sided Student's t test with a threshold of 99%. Negative 500-hPa height anomalies of over 80 m centered locally in the region of maximum growth are present as long as 120 h before the time of maximum tropopause cyclone growth (not shown). At 48 h before the time of maximum tropopause cyclone growth, these negative 500-hPa height anomalies grow to over 120 m locally in the same region (Fig. 2a). This pattern remains largely unchanged until the time of maximum tropopause cyclone growth, with negative anomalies increasing to over 160 m (Fig. 2b). These results suggest that no common large-scale circulation pattern precedes cyclonic TPV intensification at locations distant from the vortex. The possibility that local factors, rather than large-scale circulation anomalies, are responsible for TPV intensity changes motivates a case study investigation of a TPV in order to examine vortex-scale processes from a PV framework.

3. PV diagnostics

Theory and methodology

Vortex intensity changes can be quantified using the Ertel PV tendency equation (e.g., Pedlosky 1998):

$$\frac{D\Pi}{Dt} = \frac{D}{Dt}\left(\frac{1}{\rho}\boldsymbol{\omega}_a \cdot \nabla\theta\right) = \frac{\boldsymbol{\omega}_a}{\rho} \cdot \nabla\frac{D\theta}{Dt} + \frac{\nabla\theta}{\rho} \cdot \left(\nabla \times \frac{\mathbf{F}}{\rho}\right). \quad (1)$$

Here,

$$\frac{D}{Dt} = \frac{\partial}{\partial t} + u\frac{\partial}{\partial x} + v\frac{\partial}{\partial y} + w\frac{\partial}{\partial z}$$

is the time rate of change following the fluid,

$$\nabla = \left(\frac{\partial}{\partial x}, \frac{\partial}{\partial y}, \frac{\partial}{\partial z}\right)$$

is the gradient operator, ρ is the density, $\mathbf{U} = (u, v, w)$ is the three-dimensional velocity vector, and $\mathbf{F}$ is the frictional force vector on momentum. The three-dimensional absolute vorticity vector is given by $\boldsymbol{\omega}_a = \boldsymbol{\omega} + 2\boldsymbol{\Omega} = \nabla \times \mathbf{U} + 2\boldsymbol{\Omega}$, where $\boldsymbol{\Omega}$ is the earth's rotational vector, and

$$\Pi = \frac{1}{\rho}\boldsymbol{\omega}_a \cdot \nabla\theta$$

is the Ertel PV (EPV). Potential temperature is given by

$$\theta = T\left(\frac{p_o}{p}\right)^{R/c_p},$$

where T is temperature, p is pressure, $p_o = 10^5$ Pa is a standard constant, $R = 287$ J K^{-1} kg^{-1} is the dry air gas constant, and $c_p = 1004$ J K^{-1} kg^{-1} is the specific heat capacity of dry air at constant pressure. Given the PV-based definition of vortex amplitude adopted here, (1) implies that vortex intensity changes can only occur in the presence of diabatic or frictional processes.

In the numerical modeling experiments described below, changes in EPV are determined following the vortex as defined by the area within the last closed contour of potential temperature on the 2-PVU surface. This technique will be used to quantify changes in vortex strength by evaluating (1) within the location of a closed tropopause potential temperature contour through a deep layer of the atmosphere. Diabatic tendencies in the numerical model derive from tendencies due to radiation, latent heating, planetary boundary layer processes (i.e., sensible and latent heat fluxes, local and nonlocal boundary layer mixing, and entrainment), cumulus parameterization, and dissipation, which are denoted by $\dot{\theta}_{rad}$, $\dot{\theta}_{lh}$, $\dot{\theta}_{pbl}$, $\dot{\theta}_{cumulus}$, and $\dot{\theta}_{mix}$, respectively, where $\dot{\theta}$ is the heating represented as a material change in potential temperature. The thermodynamic equation then takes the following form:

$$\frac{D\theta}{Dt} = \dot{\theta}_{rad} + \dot{\theta}_{lh} + \dot{\theta}_{pbl} + \dot{\theta}_{cumulus} + \dot{\theta}_{mix}. \quad (2)$$
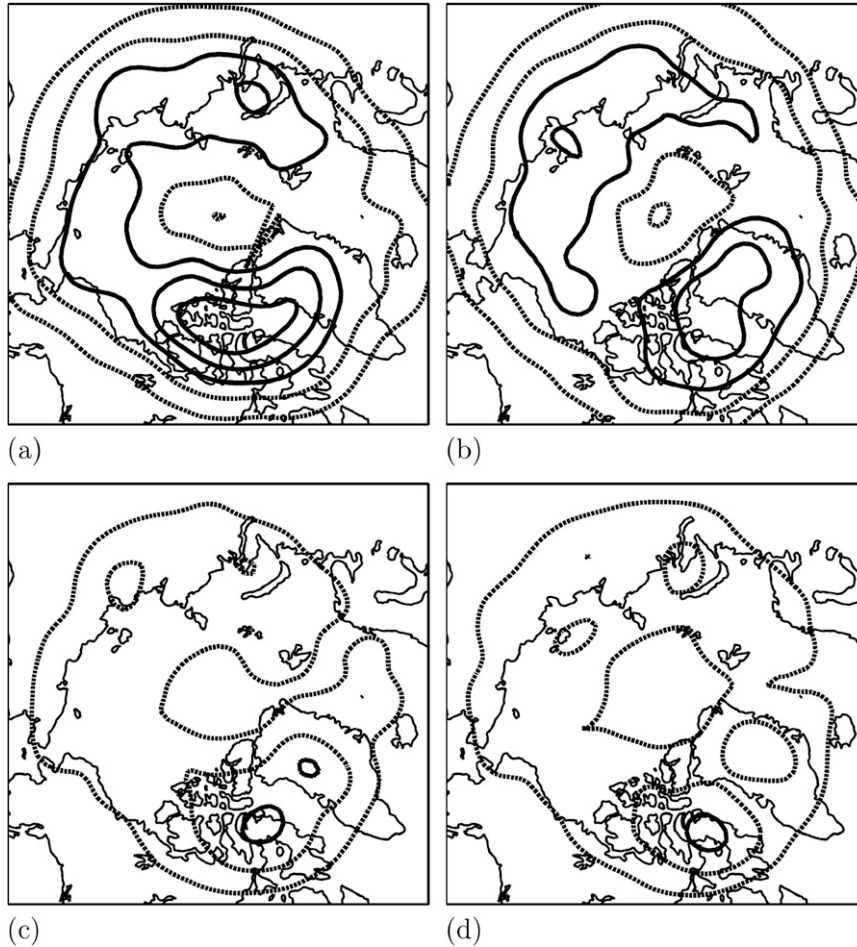
FIG. 1. Area-weighted occurrence of tropopause polar (a) cyclogenesis, (b) cyclolysis, (c) cyclone growth, and (d) cyclone decay during the period 1948–99. Values are equal to the number of unique vortices within a 5° latitude × 15° longitude box divided by the cosine of latitude (contour interval of 100). Dashed lines correspond to the 100 and 200 contours while solid lines correspond to the 300, 400, and 500 contours. Only vortices lasting at least 2 days and that spent at least 60% of their lifetimes north of 65°N latitude are considered.

The tendency terms on the right-hand side of the above equation can be used to calculate EPV tendencies due to the first right-hand-side term of (1). Similarly, the frictional force vector on momentum **F** can be used to calculate EPV tendencies due to the second right-hand-side term of (1) when evaluating errors in the diabatic EPV tendencies described subsequently.

To estimate the error in the EPV tendency budget both advection and time tendency terms must be evaluated, and errors in these estimates can be large since EPV is not a model state variable. We are most interested in an estimate of the error in the diabatic EPV tendency, and adopt the following strategy to estimate that quantity. To eliminate the advection and time tendency terms from the error estimate, a separate "adiabatic" integration is performed as described below.

Errors, defined as budget residuals, can then be quantified for both the full-physics integration and the adiabatic integration by

$$R = \left[\frac{\partial \Pi}{\partial t} + \mathbf{U} \cdot \nabla \Pi\right] - \frac{\boldsymbol{\omega}_a}{\rho} \cdot \nabla \frac{D\theta}{Dt} - \frac{\nabla\theta}{\rho} \cdot \left(\nabla \times \frac{\mathbf{F}}{\rho}\right) \quad (3)$$

and

$$R_a = \left[\frac{\partial \Pi}{\partial t} + \mathbf{U} \cdot \nabla \Pi\right]_a, \quad (4)$$

respectively. The terms inside the square brackets on the right-hand side of the above equations represent the EPV time tendency and advection terms. We calculate both terms from model output using centered finite differences in space and third-order finite differences in
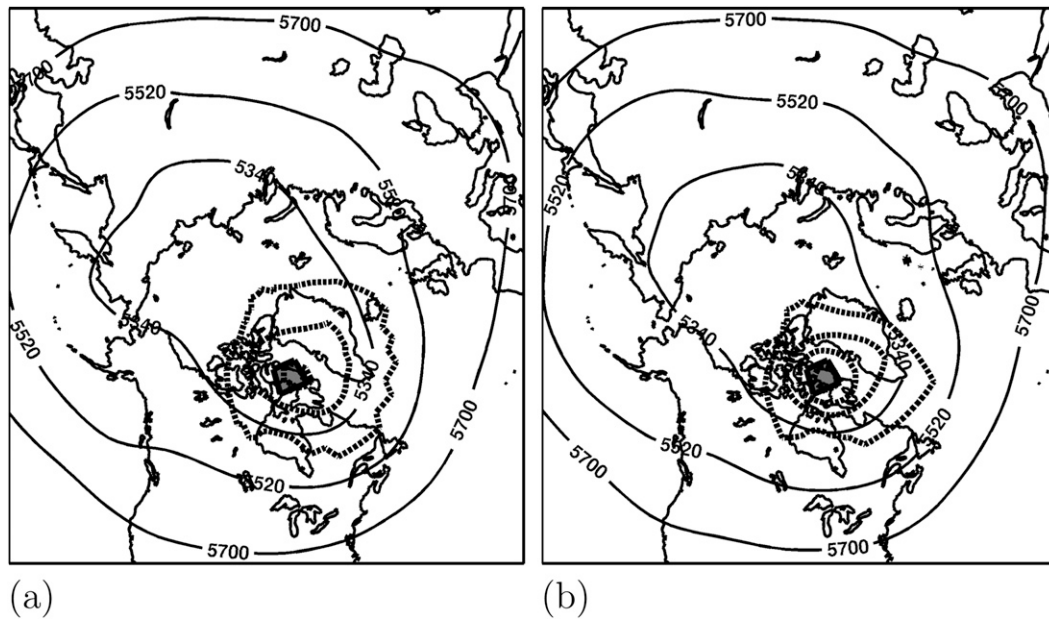
FIG. 2. Time evolution of the sample-mean 500-hPa geopotential height (thin solid lines) and geopotential height anomalies [heavy solid (dashed) lines for positive (negative) anomalies every 40 m] (a) 48 and (b) 0 h before the time of maximum tropopause cyclone growth centered at 70°N, 74°W. The zero contour is suppressed in the anomaly fields, and all anomalies are statistically significant at the 99% confidence interval using a two-sided Student's t test. The shaded region is the 5° latitude × 15° longitude box surrounding the location with the maximum tropopause cyclone growth.

time. The second term on the right-hand side of (3) is the EPV tendency due to diabatic processes, which we will also refer to as the diabatic term, and the third term on the right-hand side of (3) is the EPV tendency due to the frictional force on momentum, which we will refer to as the frictional term. To evaluate these equations, model restart files[2] are created every 6 h during the course of the model simulations. Using these restart files, the model is integrated for 30 min using an output interval equal to the model time step. Every term in the PV budget is evaluated offline at each model step (120 s). These results are then averaged over each of the 30-min restart simulation periods yielding one value for each term every 6 h.

The adiabatic residual, R_a, is derived by the process just described, but for an integration of the model without diabatic or frictional processes. Note that some sources of error, such as implicit model diffusion (due to the time integration scheme), and grid interpolation, are difficult to estimate and are not explicitly considered here. Since estimates of the time derivative and advection terms are leading sources of error common to both R_a and R, we define the diabatic residual as the differ-

ence between (3) and (4), $R_d = R - R_a$, which isolates an estimate of the part of the error due only to the diabatic tendency.

Before proceeding to the results, we provide a cartoon sketch to anticipate the primary patterns associated with radiation and latent heating tendencies. Clouds play an important role in how radiation is redistributed in the atmosphere (e.g., Turner 2005), which in turn affects how potential vorticity is redistributed. Since the Arctic is characterized by low temperature and widespread cloudiness (e.g., Curry et al. 1996), we expect that near the tropopause, the dominant diabatic contributions to the PV budget are from radiation and latent heating. Considering this expectation and only the vertical component of vorticity for the purposes of this illustration, then using (2), (1) simplifies to

$$\frac{D\Pi}{Dt} \simeq \frac{\zeta_a}{\rho}\frac{\partial}{\partial z}(\dot{\theta}_{\text{rad}} + \dot{\theta}_{\text{lh}}),$$

where $\zeta_a = \zeta + f$ is the absolute vertical vorticity composed of the relative vorticity ζ and planetary vorticity f. The vertical structure of the EPV tendencies are proportional to vertical gradients of latent heating and radiation, scaled by the absolute vorticity. Figure 3 shows a schematic of the expected cloud–radiative feedback

_____

[2] These files contain all information needed to continue integrating the model from a point in time, accurate to round-off error.
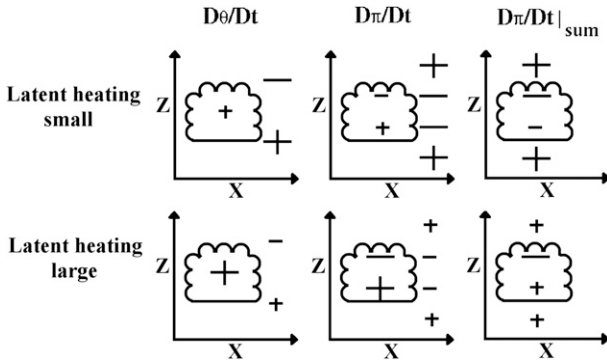
FIG. 3. Schematic illustrating the relative importance of latent and radiational heating on potential vorticity tendency near clouds. (top) The case when latent heating is relatively small compared to radiational heating and (bottom) the case where latent heating is relatively large compared to radiational heating. Here plus signs represent positive values, minus signs represent negative values, and magnitudes are denoted by relative size of the symbols. (left) The total heating ($D\theta/Dt$), where symbols inside the cloud represent latent heating and outside the cloud represent radiational heating. (middle) The independent EPV tendencies ($D\pi/Dt$), where symbols inside the cloud represent EPV tendencies from latent heating and outside the cloud represent EPV tendencies from radiation. (right) The net EPV tendency ($D\pi/Dt|_{\text{sum}}$) resulting from the combined effects of latent and radiational heating.

processes that affect PV. If latent heating is relatively small in comparison with cloud-top radiational cooling, a positive EPV tendency is expected just above the cloud top. Conversely, when latent heating is relatively large with respect to radiation, a negative EPV tendency is expected near the cloud top. We hypothesize that in the Arctic, vortex intensification occurs when radiative tendencies dominate latent heating tendencies which, by the Clausius–Clapeyron equation, is more likely at colder temperatures typical of the Arctic than at other locations.

4. Case study

The cyclonic TPV under consideration occurred during the 37-day period from 1 November to 7 December 2005, and is identified following the local minimum in tropopause potential temperature derived from the Global Forecast System (GFS) analyses (Fig. 4a); for clarity, only the first 25 days of the vortex track are shown. This case was chosen primarily because it has large amplitude, which enhances the signal-to-noise ratio, and also because it was sampled directly by radiosonde observations, which provide a rare check on the structure and intensity of the TPV. A secondary consideration is that the event is very long lived, with distinct and well-separated intensification and weakening
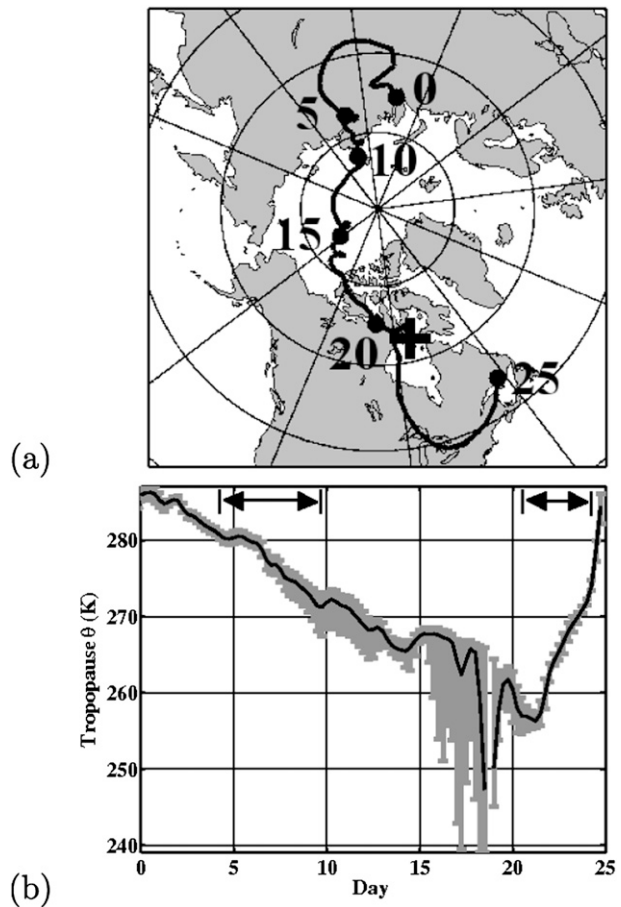

FIG. 4. GFS tropopause analysis of the TPV cyclone during 1–26 Nov 2005. (a) Vortex track following the minimum tropopause potential temperature values on the 2-PVU surface and (b) corresponding time series of the average of the minimum 10 tropopause potential temperature values with the shaded areas representing a range of tropopause definitions from 1.75 to 2.25 PVU; this range provides a measure of sensitivity to the tropopause definition. Solid circles in (a) denote days since the beginning of the vortex track, which also correspond to the abscissa in (b). A 1–2–1 smoother is applied to the time series and values below 245 K are suppressed. In (a), the Coral Harbour, Nunavut, Canada radiosonde station location is denoted with the boldface plus sign. In (b), arrows indicate the time periods considered in the model simulations discussed in section 4.

phases, which facilitates independent numerical simulations of these portions of the life cycle; from a climatological perspective, it is atypical in this regard. The vortex originates over Siberia and travels slowly, nearly in a loop, arriving on the northern Siberia coast near the Taymyr Peninsula after one week. The vortex continues to move slowly northward for another week, at an average speed of 5–10 m s^{-1}, remaining near the central Arctic Ocean. It reaches the northwestern Canadian Archipelago on day 18 of its life cycle, thereafter accelerating, turning southeast, and reaching Hudson

Bay by day 21. The vortex performs a loop pattern between the Great Lakes and Hudson Bay, and by day 37 can no longer be tracked by the presence of closed tropopause potential temperature contours near the northeastern U.S. Atlantic coast.

The corresponding time series of vortex-core potential temperature (using the average of the 10 lowest values around the minimum value), from 1 November (day 0) to 26 November 2005 (day 25) is shown in Fig. 4b. Tropopause potential temperature steadily decreases for about 17 days, reflecting an intensifying cyclone. From days 17 to 22 there are large fluctuations, which we speculate are due to the low tropopause interacting with an Arctic low-level temperature inversion, a commonly observed feature in this region (e.g., Curry 1983). The close proximity of the tropopause and low-level temperature inversion is apparent in a radiosonde observation near the vortex core on day 23 (Fig. 5c), where the tropopause and top of the low-level temperature inversion are separated by less than approximately 200 hPa. Tropopause potential temperature values of around 260 K and tropopause pressure values near 800 hPa reflect an intense vortex at this time. A transition from strengthening to weakening begins around day 22. During this time, the cyclone moves southward over Hudson Bay, and a significant surface low pressure center forms.

A sequence of radiosonde profiles at Coral Harbour, Nunavut, Canada and the corresponding GFS tropopause analyses capture the vortex vertical structure near Hudson Bay (Fig. 5). Before the cyclone reaches Coral Harbour, the observed tropopause pressure is approximately 350 hPa with westerly winds reflecting a cyclonic circulation located north of the station (Figs. 5a,b), and nearly saturated conditions from the top of the surface inversion to the tropopause (Fig. 5a). At 0000 UTC 22 November 2005, the cyclone is closest to the Coral Harbour radiosonde station, with a tropopause pressure of 650 hPa, compared to 675 hPa in the GFS analysis (Figs. 5c,d). At the surface, the passage of a cold front at Coral Harbour decreases surface temperatures there by about 12°C during this 24-h period while the somewhat drier, but nearly moist adiabatic temperature structure remains in the free troposphere (Fig. 5c). Furthermore, the layer between the top of the surface layer and tropopause is only ~200 hPa, or about 375 hPa less than at the same location 24 h earlier (Figs. 5a,c). The maximum tropopause pressure of 807 hPa is located north of the station in the GFS analysis (Fig. 5d). As the vortex moves southward over Hudson Bay, the tropopause pressure at Coral Harbour slowly rises (Figs. 5e–h) and a surface low pressure system intensifies over Hudson Bay. The surface inversion also

strengthens during this time and the surface layer becomes nearly saturated, while the free-tropospheric layer above dries out significantly (Figs. 5e,g). A surface low, with a minimum sea level pressure of 987 hPa in the GFS analysis, develops when the vortex moves over Hudson Bay. This surface low pressure system appears similar to a case examined by Albright et al. (1995), who found that its formation was a result of convective latent heat release when an upper-level cold-core low pressure system moved over a relatively warm, ice-free segment of Hudson Bay, enhancing surface heat and moisture fluxes. In the present case, a complex surface low pressure structure is evident in a Moderate Resolution Imaging Spectroradiometer (MODIS; Fig. 6) with a cyclonic arc of clouds found over southwestern Hudson Bay.

5. Numerical simulation and PV budget

Numerical simulations are performed for two stages in the life cycle of the case just described. Using the GFS analyses as a guide, we choose to examine days 4–9 in the first simulation to analyze the vortex intensification phase over Siberia, and days 21–24 in the second simulation to examine the vortex weakening phase over Hudson Bay (Fig. 4b). We note that although the vortex-core potential temperature exhibits an increase (weakening) during the second phase (Fig. 4b), area averages shown subsequently over the entire vortex reveal little change in intensity; nevertheless, we shall refer to this time as the weakening phase. These simulations are used to estimate the diabatic terms in the PV budget as described in section 3.

a. Numerical model

We use the Advanced Research Weather (ARW) version of the Weather Research and Forecasting (WRF) model, version 2.1.2 (Skamarock et al. 2005), and the WRF Standard Initialization (WRF-SI), version 2.1. Time integration is achieved by a third-order accurate Runge–Kutta method, and horizontal advection by a fifth-order accurate scheme. A horizontal grid spacing of $\Delta x = \Delta y = 30$ km is used, with 31 vertical levels and a model time step of $\Delta t = 120$ s. The following physics schemes are used: Rapid Radiative Transfer Model (RRTM) longwave radiation (Mlawer et al. 1997), the National Aeronautics and Space Administration (NASA) Goddard shortwave radiation (Chou and Suarez 1994), WRF single-moment (WSM) 5-class microphysics (Hong et al. 2004), Kain–Fritsch cumulus convection (Kain and Fritsch 1993), Yonsei University (YSU) planetary boundary layer (Hong and Pan 1996), thermal diffusion surface physics (Chen and Dudhia 2001a,b),
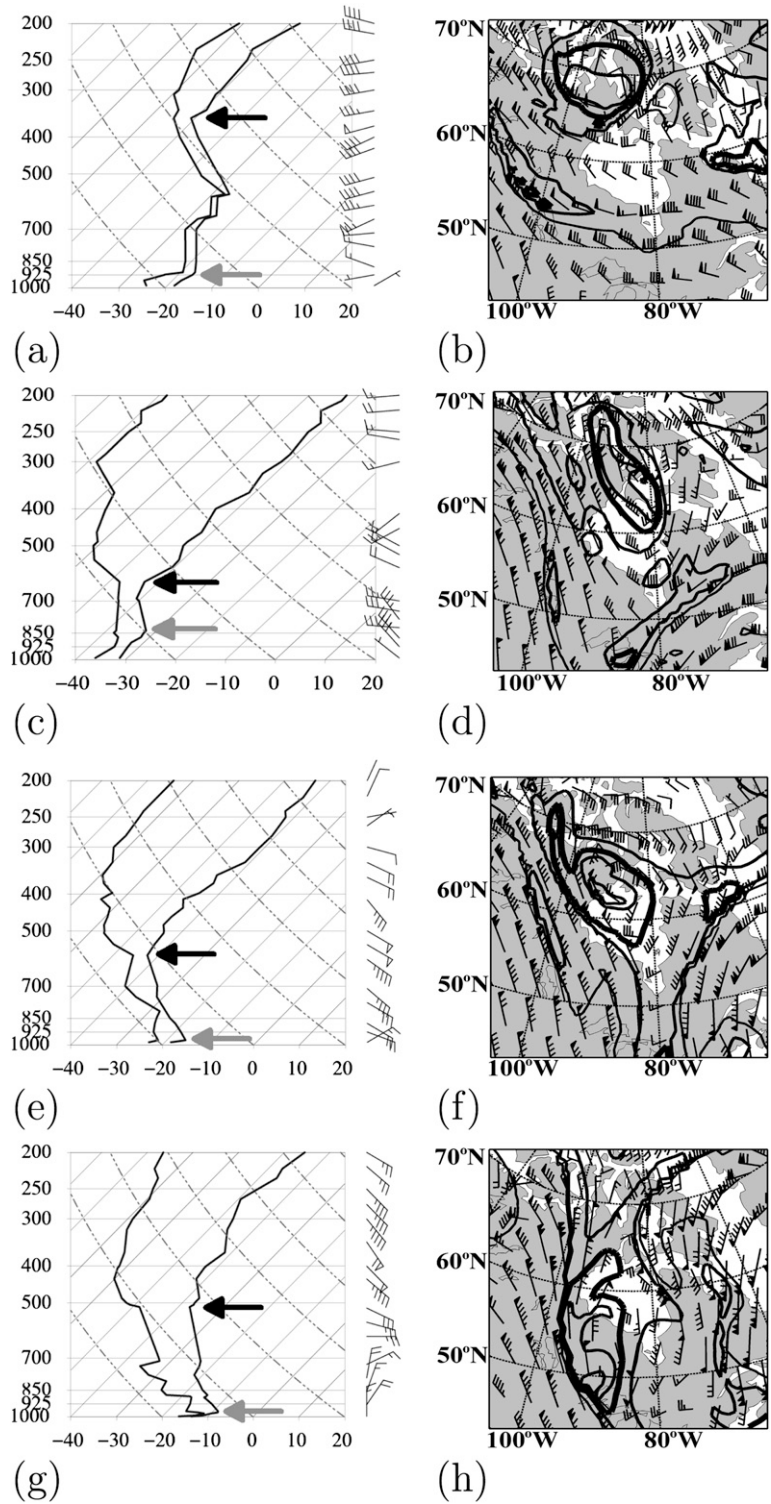
FIG. 5. (left) Skew T–log$p$ diagram of radiosonde profiles of temperature (°C) and dewpoint temperature (°C) at Coral Harbour, Nunavut, Canada and (right) GFS tropopause pressure (contours every 100 hPa with the 500-hPa contour shown bold for reference) and tropopause wind (kt) at 0000 UTC (a),(b) 21; (c),(d) 22; (e),(f) 23; and (g),(h) 24 Nov 2005. The Coral Harbour radiosonde location is shown in Fig. 4a. (left) The gray arrow marks the location of the top of the surface inversion layer, and the black arrow marks the location of the tropopause.
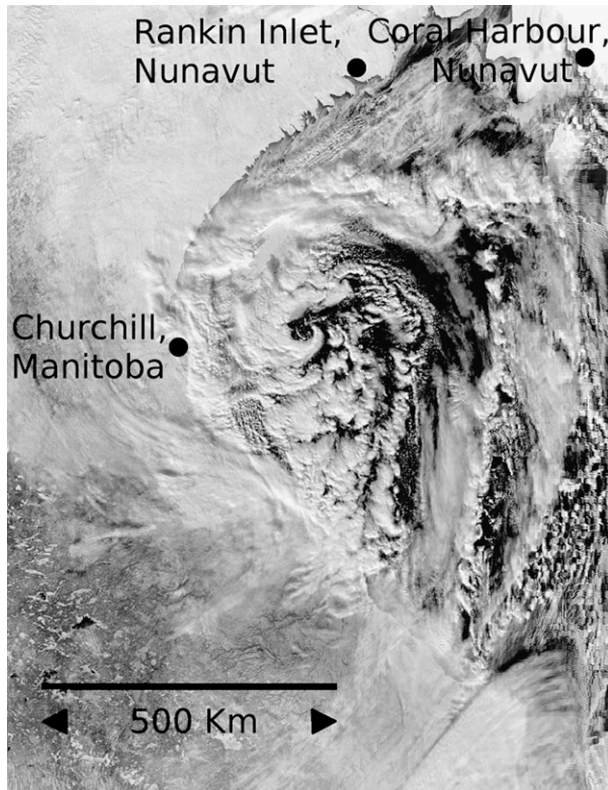
FIG. 6. MODIS visible satellite image from 1845 UTC 23 Nov 2005. Field of view is the western side of Hudson Bay.
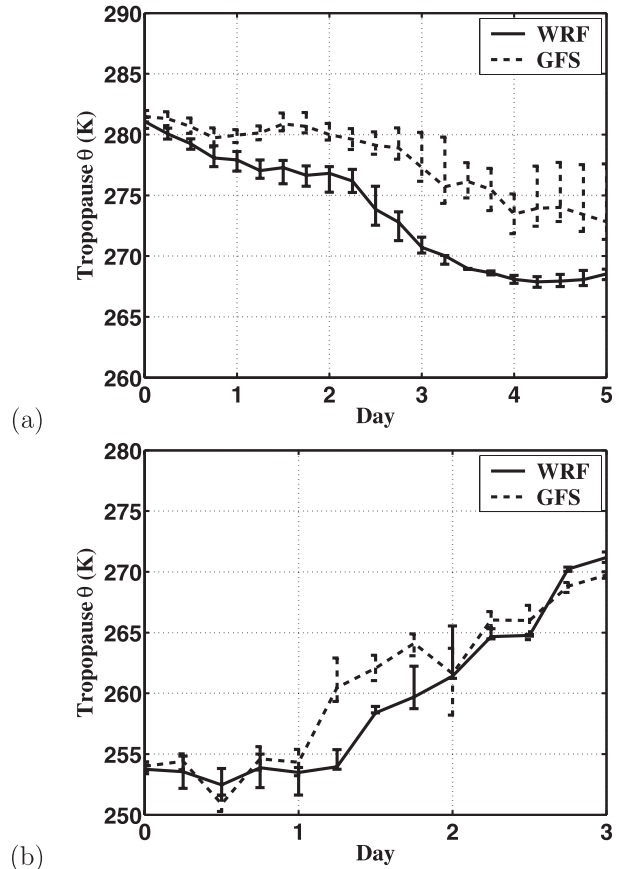

(a)

(b)

FIG. 7. Tropopause potential temperature (K) at the vortex core from GFS analyses (dashed lines) and WRF simulations (solid lines) initialized (a) 0000 UTC 5 Nov 2005 over Siberia, Russia, and (b) 0000 UTC 22 Nov 2005 over Hudson Bay, Canada. Vertical bars represent values derived from tropopause definitions ranging from 2.25 to 1.75 PVU.

and Monin–Obukhov surface layer physics (Paulson 1970; Dyer and Hicks 1970; Webb 1970).

The strengthening and weakening phases that are simulated here occur while the vortex is over Siberia and near Hudson Bay, respectively, and will be referred to as the Siberia and Hudson Bay segments. Forecasts are initialized using GFS analyses at 0000 UTC 5 November 2005 for the Siberia segment and at 0000 UTC 22 November 2005 for the Hudson Bay segment, with boundary conditions derived from 6-hourly GFS analyses and intervening 3-h forecasts. The simulations are performed on a polar stereographic map projection, with a center of 74°N, 107°E for the Siberia simulation, and 57°N, 84°W for the Hudson Bay simulation. There are 100 x and y grid points in the Siberia simulation and 100 $x \times 144$ y grid points in the Hudson Bay simulation.

b. Intensification phase PV budget

In terms of tropopause vortex-core potential temperature, both the WRF forecast and GFS analysis show a deepening cyclonic vortex for the Siberia segment (Fig. 7a). Time–height sections of the EPV tendency due to all contributions from (1) are shown in Fig. 8 for the days corresponding to those in Fig. 7a. Each indi-

vidual diabatic contribution to the total EPV tendency is obtained by considering its individual contribution to (2) and combining this result with the first term in the right-hand side of (1). Recall that all diabatic and frictional tendencies are calculated in their respective physical or microphysical numerical scheme as described in the previous section, and we obtain their instantaneous values from model output. All fields are averaged spatially for tropopause potential temperature below 285 K locally within the vortex, which represents approximately the last closed contour surrounding the vortex throughout the entirety of the simulation. Using the full diabatic tendency term in (2) with the first term on the right-hand side of (1), the net diabatic effect is the creation of positive EPV near the tropopause, with the tropopause lowering in time from approximately 490 initially to 570 hPa by day 4 (Fig. 8a). Cloud water (sum of liquid and ice mixing ratios) reveals that clouds
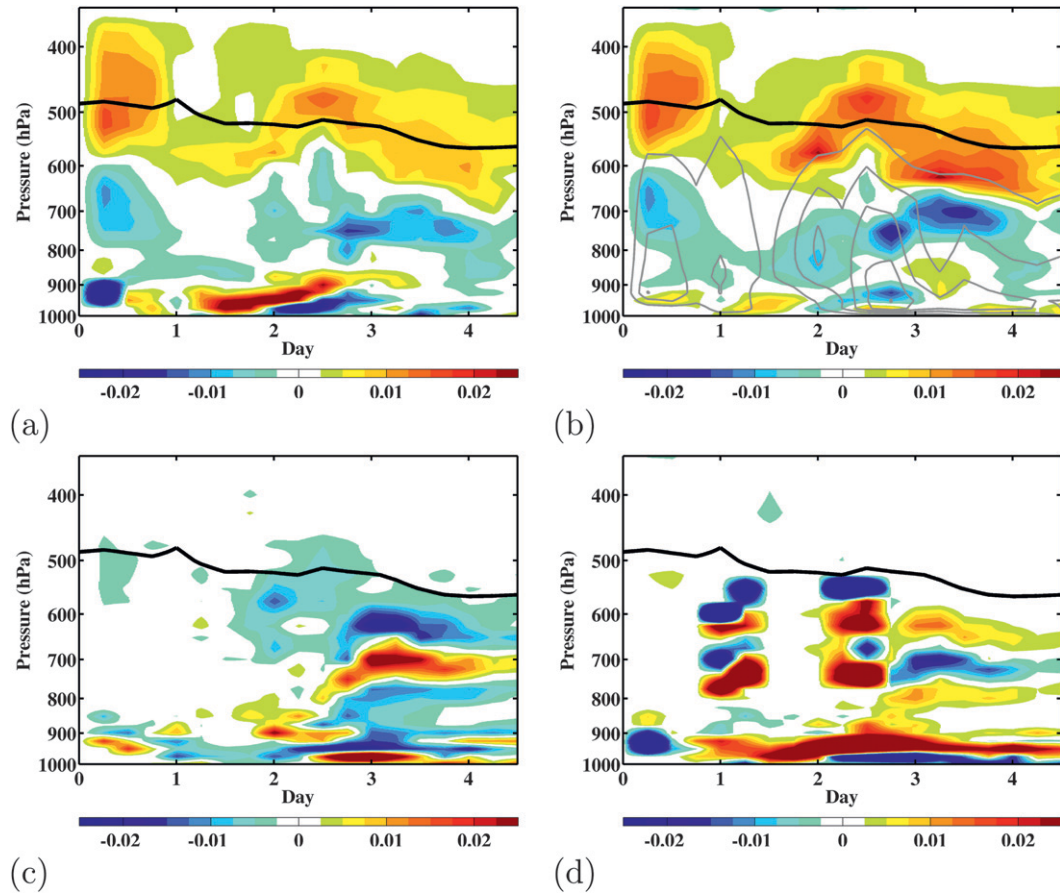
FIG. 8. Time–height sections from a WRF simulation during 0000 UTC 5 Nov 2005–0000 UTC 10 Nov 2005 of the EPV tendency (PVU h^{-1}) due to (a) all diabatic processes, (b) radiation (colors) and cloud water (sum of liquid and ice mixing ratios; contours every 0.004 g kg^{-1}), (c) latent heating, and (d) the sum of the planetary boundary layer scheme, cumulus scheme, and frictional processes. All fields are averaged within the area encompassed by the 285-K closed tropopause potential temperature contour. The thick black line represents the 2-PVU surface. Labels on the abscissa are days from the start of the simulation. EPV tendency color interval is 0.0025 PVU h^{-1}.

extend throughout the troposphere, and EPV generation from the radiational diabatic component is concentrated near the top of the clouds, primarily near the tropopause (Fig. 8b). Latent heating contributes to EPV destruction in the upper troposphere and to some extent near the tropopause; however, the most negative EPV tendencies are found below the tropopause (Fig. 8c). The results show that, for the chosen case, the tendency to create EPV from cloud-top radiational cooling dominates the tendency to destroy EPV from latent heating.

Time-mean vertical profiles of EPV tendency components for this segment averaged over the times shown in Fig. 8 (5–10 November 2005) indicate that the largest EPV tendency near the tropopause comes from advection, followed by the full diabatic term (Fig. 9a). Decomposing the full diabatic term shows that the most significant diabatic component near the tropopause is due to radiation, which accounts for nearly all of the total diabatic term (Fig. 9b). EPV destruction due to latent heating peaks 75 hPa below the tropopause, whereas creation of radiational EPV peaks closer to the tropopause, which is qualitatively consistent with the conceptual picture given in Fig. 3a, where radiational effects were assumed to dominate latent heating effects. The diabatic residual is mainly positive in the troposphere, and much smaller than the radiation and latent heating tendencies, which lends confidence to these results.

c. Weakening phase PV budget

The WRF forecast and GFS analysis both show vortex-core tropopause potential temperature increasing, which indicates a weakening cyclonic vortex during the Hudson Bay simulation (Fig. 7b). In this analysis, all fields are averaged spatially and locally within the vortex as in the Siberia simulation, but for tropopause
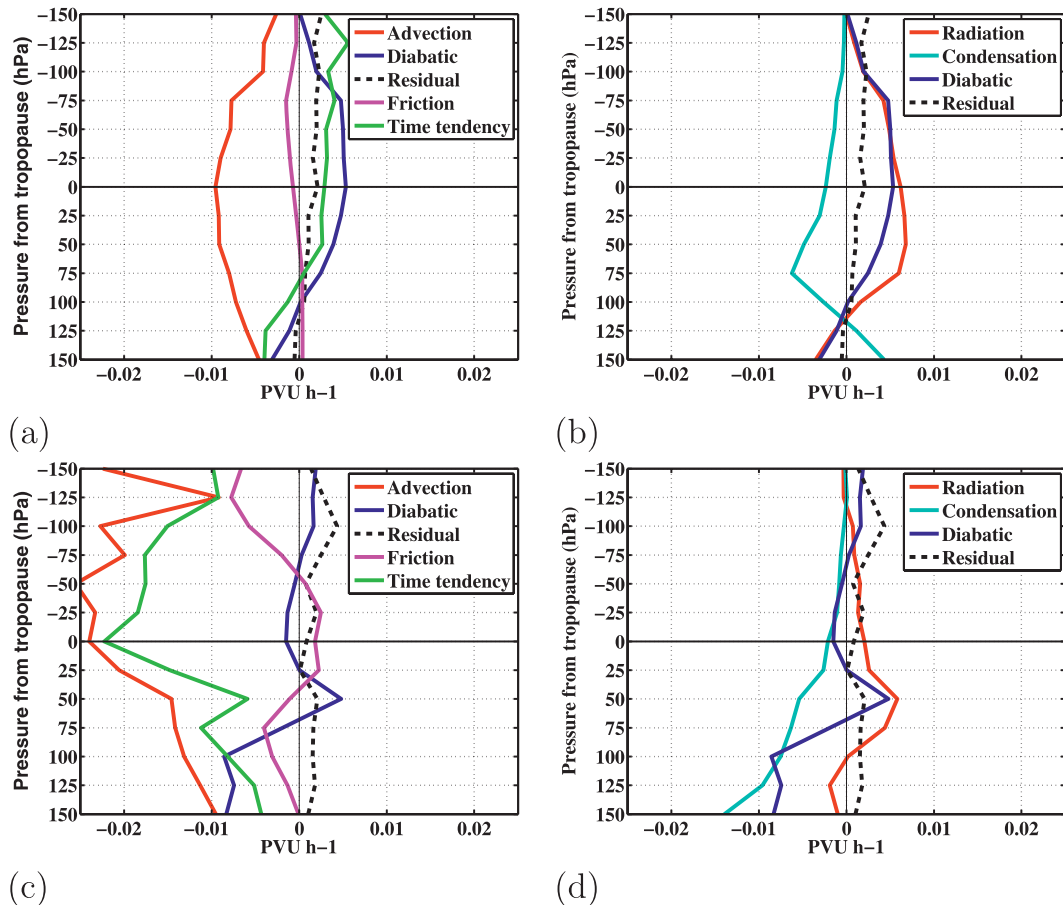
FIG. 9. Time-mean vertical profiles of the EPV tendency (PVU h^{-1}) from (left) all components and (right) diabatic contributions for the (a), (b) Siberia simulation and (c), (d) Hudson Bay simulation from Eqs. (3) and (4). The term labeled "advection" is $-\mathbf{U}\cdot\nabla\Pi$ in Eq. (3); "diabatic" is the second term on the right-hand side of (3); "residual" is the diabatic residual estimate of the error in the diabatic EPV terms, R_d, from (3) and (4); "friction" is the third term on the right-hand side of (3); and "time tendency" is $\partial\Pi/\partial t$ from (3). Vertical levels are pressure coordinates (hPa) relative to the tropopause; zero denotes the tropopause. All values are averaged within the 285-K tropopause potential temperature contour for the Siberia simulations and 280 K for the Hudson Bay simulation.

potential temperature values below 280 K, which represents the last closed tropopause potential temperature contour during this phase. Time–height sections do not show significant contributions to EPV tendency from diabatic effects near the tropopause (Fig. 10a). The tropopause height remains relatively unchanged near 600 hPa, and although cloud mass extends throughout the troposphere, the main concentration is in the lower troposphere near 850 hPa (Fig. 10b). Moreover, cloud mixing ratios are higher in this segment compared to the Siberia segment, and the clouds are also composed mainly of supercooled liquid drops, rather than ice crystals as in the Siberia segment (not shown). Radiation contributes to weak positive EPV tendencies in the upper troposphere (Fig. 10b). A dipole of EPV tendency straddles the maximum in cloud mass near 850

hPa, with weak negative tendencies in the upper troposphere (Fig. 10c). This dipole EPV tendency pattern appears consistent with the pattern for a midlatitude baroclinic low pressure system documented by Stoelinga (1996), where an EPV tendency due to latent heating of about -0.09 PVU h^{-1} centered around 700 hPa was observed. Latent heating contributes to a dipole pattern centered on the maximum cloud mass, with EPV destruction in the upper troposphere (Fig. 10c). Diabatic tendencies from the remaining terms (i.e., planetary boundary layer processes, convection, and dissipation) are complicated, but affect PV mainly in the lower troposphere (Fig. 10d).

Time-mean vertical profiles of EPV tendency components for this segment averaged over the times shown in Fig. 10 (22–25 November 2005) indicate that the
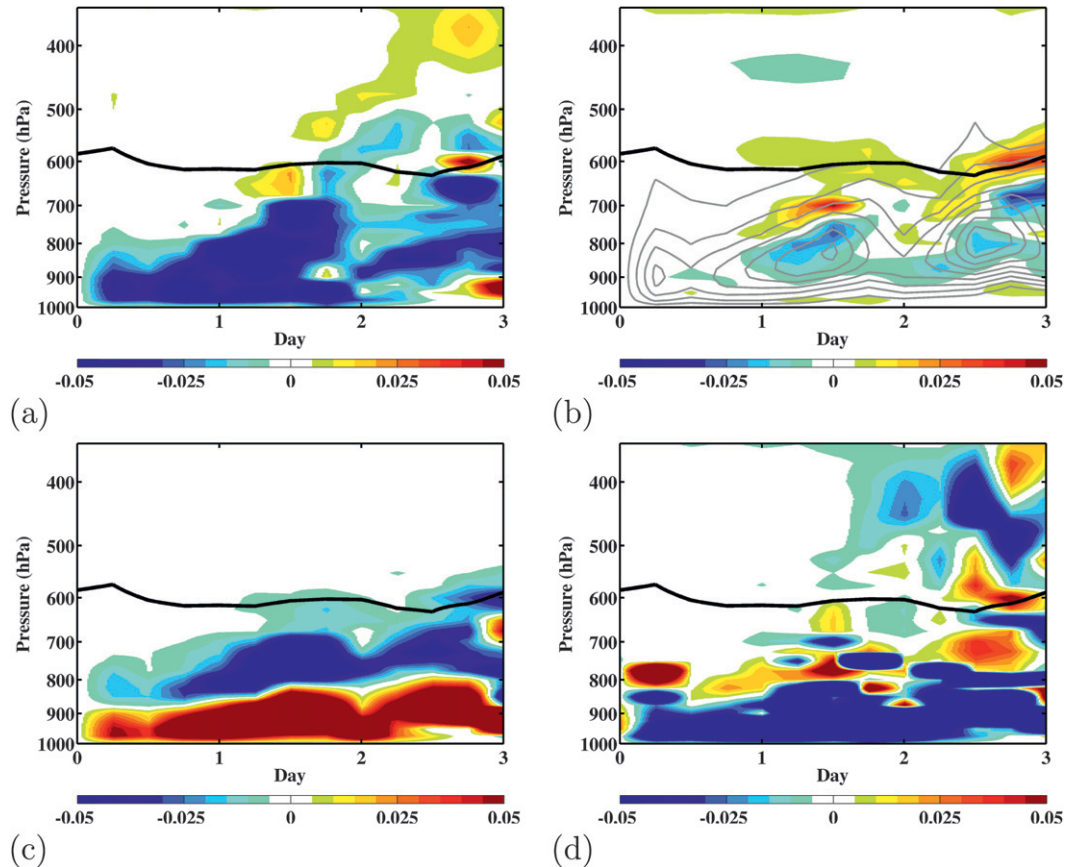
FIG. 10. As in Fig. 8, but for the Hudson Bay simulation from 0000 UTC 22 Nov to 1200 UTC 24 Nov 2005 and all fields are averaged within the 280-K tropopause potential temperature contour.

advection and time tendency terms dominate the budget near the tropopause, and that the diabatic component is comparatively small (Fig. 9c). Note that away from the tropopause, values are not easily comparable to the values in the Siberia simulation (cf. Figs. 9a,b with 9c,d), as the depth of the free troposphere differs between these two segments of the vortex life cycle. Profiles of the individual diabatic terms are more complex during this time period compared to the Siberia segment, with most diabatic components making comparably sized contributions near the tropopause (Fig. 9d). Moreover, the diabatic residual term is of comparable magnitude to the full diabatic term as well as individual diabatic components, suggesting that the results are less conclusive than for the Siberia segment.

6. Summary and concluding remarks

Diabatic mechanisms that affect the intensity of a cyclonic tropopause polar vortex (TPV) have been quantified in a potential vorticity framework. Motivation for the case study was derived from an Arctic

vortex census, which showed that the maximum occurrence of tropopause cyclogenesis, cyclolysis, growth, and decay are found near Baffin Island, Canada. Moreover, the fact that no significant relationship was found between large-scale circulation patterns and vortex intensity suggests that local processes are most important in many cases. A long-lived case was selected for closer examination, including a review of observational evidence for the event and a potential vorticity diagnosis of the strengthening and weakening phases of the vortex life cycle.

Given that latent heating typically peaks well below the tropopause, reducing potential vorticity near the tropopause, we hypothesized that cloud-top radiational cooling is important for increasing potential vorticity near the tropopause. Results from the case study provide supporting evidence for this hypothesis during the time of observed intensification. Later in the life cycle of the event, when the vortex is located over the unfrozen water of Hudson Bay, latent heating increases, primarily in the lower troposphere. The small loss in potential vorticity near the tropopause is nearly offset by a small

positive tendency from radiation, resulting in little change in the location of the tropopause averaged over the vortex area, consistent with the observed tendency.

Although a complete EPV budget has not been shown in previous studies, several studies have estimated the EPV tendency from latent heating in cold-core midlatitude cyclonic systems (e.g., Davis and Emanuel 1991; Davis 1992; Stoelinga 1996; Lackmann 2002); For example, Stoelinga (1996) showed an EPV tendency due to latent heating in the upper troposphere similar to the pattern observed in this study, with latent heating acting to destroy PV in the upper troposphere above the level of maximum latent heating. Previous theoretical considerations suggest that EPV near the tropopause depends sensitively on the combined effects of radiation, tending to create upper-level EPV, and latent heating, tending to destroy upper-level EPV (e.g., Wirth 1995). The results for the case examined here are consistent with these ideas.

It remains for future work to determine the generality of the results determined for the case study presented here. The results suggest that cyclonic tropopause vortex intensification is favored for low temperatures, since latent heating decreases approximately exponentially with temperature. This implies that the population characteristics of these ubiquitous, persistent features of the Arctic may change for a warmer Arctic climate. Idealized simulations, which provide more control and freedom than do simulations of observed cases, seem particularly relevant to address these questions. Other open questions that appear fruitful for future research include genesis, seasonality, and sensitivity to surface boundary conditions (i.e., land, ice, and open water). Moreover, these questions may help provide important insight into the changes that could incur in TPV characteristics with the changing Arctic climate system. Finally, from a predictability standpoint, the impact of these vortices on midlatitude weather would be interesting to examine, especially given their relatively small scale, episodic longevity, and potential to excite surface cyclones.

REFERENCES

Albright, M. D., R. J. Reed, and D. W. Ovens, 1995: Origin and structure of a numerically simulated polar low over Hudson Bay. *Tellus,* **47A,** 834–848.

Chen, F., and J. Dudhia, 2001a: Coupling an advanced land surface–hydrology model with the Penn State–NCAR MM5 modeling system. Part I: Model implementation and sensitivity. *Mon. Wea. Rev.,* **129,** 569–585.

——, and ——, 2001b: Coupling an advanced land surface–hydrology model with the Penn State–NCAR MM5 modeling system. Part II: Preliminary model validation. *Mon. Wea. Rev.,* **129,** 587–604.

Chou, M.-D., and M. J. Suarez, 1994: An efficient thermal infrared radiation parameterization for use in general circulation models. NASA Tech. Memo. 104606, 85 pp.

Curry, J. A., 1983: On the formation of continental polar air. *J. Atmos. Sci.,* **40,** 2278–2292.

——, W. B. Rossow, D. Randall, and J. L. Schramm, 1996: Overview of Arctic cloud and radiation characteristics. *J. Climate,* **9,** 1731–1764.

Davis, C. A., 1992: A potential-vorticity diagnosis of the importance of initial structure and condensational heating in observed extratropical cyclogenesis. *Mon. Wea. Rev.,* **120,** 2409–2428.

——, and K. A. Emanuel, 1991: Potential vorticity diagnostics of cyclogenesis. *Mon. Wea. Rev.,* **119,** 1929–1953.

Dyer, A. J., and B. B. Hicks, 1970: Flux-gradient relationships in the constant flux layer. *Quart. J. Roy. Meteor. Soc.,* **96,** 715–721.

Hakim, G. J., 2000: Climatology of coherent structures on the extratropical tropopause. *Mon. Wea. Rev.,* **128,** 385–406.

——, and A. K. Canavan, 2005: Observed cyclone-anticyclone tropopause asymmetries. *J. Atmos. Sci.,* **62,** 231–240.

Hong, S.-Y., and H.-L. Pan, 1996: Nonlocal boundary layer vertical diffusion in a medium-range forecast model. *Mon. Wea. Rev.,* **124,** 2322–2339.

——, J. Dudhia, and S.-H. Chen, 2004: A revised approach to ice microphysical processes for the bulk parameterization of clouds and precipitation. *Mon. Wea. Rev.,* **132,** 103–120.

Hoskins, B. J., M. E. McIntyre, and A. W. Robertson, 1985: On the use and significance of isentropic potential vorticity maps. *Quart. J. Roy. Meteor. Soc.,* **111,** 877–946.

Kain, J. S., and J. M. Fritsch, 1993: Convective parameterization for mesoscale models: The Kain–Fritsch scheme. *The Representation of Cumulus Convection in Numerical Models, Meteor. Monogr.,* No. 46, Amer. Meteor. Soc., 165–170.

Kalnay, E., and Coauthors, 1996: The NCEP/NCAR 40-Year Reanalysis Project. *Bull. Amer. Meteor. Soc.,* **77,** 437–472.

Lackmann, G. M., 2002: Cold-frontal potential vorticity maxima, the low-level jet, and moisture transport in extratropical cyclones. *Mon. Wea. Rev.,* **130,** 59–74.

Mlawer, E. J., S. J. Taubman, P. D. Brown, M. J. Iacono, and S. A. Clough, 1997: Radiative transfer for inhomogeneous atmosphere: RRTM, a validated correlated-k model for the longwave. *J. Geophys. Res.,* **102** (D14), 16 663–16 682.

Nolan, D. S., and L. D. Grasso, 2003: Nonhydrostatic, three-dimensional perturbations to balanced, hurricane-like vortices. Part II: Symmetric response and nonlinear simulations. *J. Atmos. Sci.,* **60,** 2717–2745.

Paulson, C. A., 1970: The mathematical representation of wind speed and temperature profiles in the unstable atmospheric surface layer. *J. Appl. Meteor.,* **9,** 857–861.

Pedlosky, J., 1998: *Geophysical Fluid Dynamics.* 2nd ed. Springer, 728 pp.

Schubert, W. H., and J. J. Hack, 1983: Transformed Eliassen balanced vortex model. *J. Atmos. Sci.,* **40,** 1571–1583.

Shapiro, L. J., and H. E. Willoughby, 1982: The response of balanced hurricanes to local sources of heat and momentum. *J. Atmos. Sci.,* **39,** 378–394.

Skamarock, W. C., J. B. Klemp, J. Dudhia, D. O. Gill, D. M. Barker, W. Wang, and J. G. Powers, 2005: A description of the advanced research WRF version 2. NCAR Tech. Note NCAR/TN-468+STR, 88 pp.

Stoelinga, M. T., 1996: A potential vorticity–based study of the role of diabatic heating and friction in a numerically simulated baroclinic cyclone. *Mon. Wea. Rev.,* **124,** 849–874.

Turner, D. D., 2005: Arctic mixed-phase cloud properties from AERI lidar observations: Algorithm and results from SHEBA. *J. Appl. Meteor.,* **44,** 427–444.

Webb, E. K., 1970: Profile relationships: The log-linear range, and extension to strong stability. *Quart. J. Roy. Meteor. Soc.,* **96,** 67–90.

Wirth, V., 1995: Diabatic heating in an axisymmetric cut-off cyclone and related stratosphere–troposphere exchange. *Quart. J. Roy. Meteor. Soc.,* **121,** 127–147.

Zierl, B., and V. Wirth, 1997: The influence of radiation on tropopause behaviour and stratosphere-troposphere exchange in an upper tropospheric anticyclone. *J. Geophys. Res.,* **102,** 883–894.